Spatial charge separation of one-dimensional $Ni_2P\text{-}Cd_{0.9}Zn_{0.1}S/g\text{-}C_3N_4$ heterostructure for high-quantum-yield photocatalytic hydrogen production

Zhixiao Qin, Fei Xue, Yubin Chen*, Shaohua Shen, Liejin Guo

International Research Center for Renewable Energy, State Key Laboratory of Multiphase Flow in Power Engineering, Xi'an Jiaotong University, Shaanxi 710049, PR China

A R T I C L E I N F O

A B S T R A C T

Constructing heterostructured photocatalysts to facilitate spatial charge separation is deemed to be central to improving photocatalytic hydrogen production. Herein, we reported the synthesis of $Ni_2P\text{-}Cd_{0.9}Zn_{0.1}S$/graphitic carbon nitride (g-C_3N_4) heterostructure for photocatalytic hydrogen production under visible-light irradiation. It was revealed that the ternary photocatalysts exhibited a one-dimensional morphology. Ni_2P nanoparticles and a layer of g-C_3N_4 were tightly deposited on the surface of $Cd_{0.9}Zn_{0.1}S$ nanorods. The optimal hydrogen evolution rate over $Ni_2P\text{-}Cd_{0.9}Zn_{0.1}S$/g-$C_3N_4$ was $\sim2100\,\mu mol\,h^{-1}\,mg^{-1}$, corresponding to an apparent quantum yield as high as 73.2% at 420 nm. Meanwhile, the g-C_3N_4 layer could effectively collect the photo-induced holes from $Cd_{0.9}Zn_{0.1}S$, which substantially alleviated the photocorrosion of metal sulfide and led to an excellent stability for 90 h. A detail analysis of the action mechanism by photoluminescence, surface photovoltage, and electrochemical measurements revealed that the dramatically improved photocatalytic activity should be ascribed to highly efficient spatial separation of photo-induced charge carriers, as well as accelerated surface reaction by Ni_2P cocatalysts. It is believed that the present work supplies an effective way to obtain non-precious heterostructured photocatalytic system for high-quantum-yield and stable hydrogen production.

1. Introduction

Since the discovery of the Honda-Fujishima effect in 1972 [1], photocatalytic hydrogen production from water has become a promising solution to global energy and environmental issues by utilizing solar energy [2–6]. However, developing highly active, low-cost, and long-term stable photocatalysts is still a great challenge to the scientific community. In a typical photocatalytic process, photocatalysts absorb the incident light to generate electrons and holes, which are separated and transferred to the surface for redox reactions. The improvement of charge separation has proven to be crucial to enhance the photocatalytic performance [7,8]. For instance, fabricating type II heterostructures, in which both the conduction band and valence band of one constituent semiconductor are either higher or lower than those of the other semiconductor, has been demonstrated as an effective way to promote the spatial charge separation and photocatalytic property

[9–14]. In this approach, the basic requirement for achieving the efficient charge separation is the formation of high-quality heterojunctions.

One-dimensional nanostructures exhibit substantial advantages compared to bulk materials due to the features of fast and long-distance electron transport, larger specific surface areas, as well as enhanced light absorption and scattering properties from high length-to-diameter ratios [15]. These advantages have promoted the application of one-dimensional nanostructures in heterojunction photocatalysis [16–18]. It is believed that the large surface area can ensure the sufficient contact between different phases, and the one-dimensional morphology can accelerate charge transport. Thus, a high-quality heterojunction can be expected based on the one-dimensional nanomaterials, leading to improved photocatalytic performance. One-dimensional $Cd_{1-x}Zn_xS$ photocatalysts have been investigated due to their unique morphology, suitable band gaps for sunlight utilization, and excellent catalytic functions [19,20]. However, an inevitable issue that metal sulfides are subjected to photocorrosion deserves our attention [21]. As an effective approach, coupling metal sulfide photocatalysts with corrosion-resisted materials (such as graphene, carbon

---

* Corresponding author.
 E-mail address: ybchen@mail.xjtu.edu.cn (Y. Chen).

nanotubes, silicas, and polymeric materials) to achieve efficient charge separation, has been demonstrated to be successful to simultaneously improve the stability and activity [22–25]. In recent years, graphitic carbon nitride (g-C_3N_4) has attracted increasing research interest as a metal-free polymeric semiconductor for photocatalytic hydrogen production due to its sufficient stability and capability of visible-light harvest [26–28]. It is found that the energy levels of g-C_3N_4 and $Cd_{1-x}Zn_xS$ are well-matched to ensure the formation of a type II heterostructure, which can promote the transfer of photoexcited electrons from g-C_3N_4 to $Cd_{1-x}Zn_xS$ and photoexcited holes from $Cd_{1-x}Zn_xS$ to g-C_3N_4 [29,30]. The separation of photo-induced charges in $Cd_{1-x}Zn_xS$/g-C_3N_4 could enable the great improvement of photocatalytic activity and effective protection of $Cd_{1-x}Zn_xS$ from self-photooxidation. On the basis of above analysis, it seems quite promising to couple one-dimensional $Cd_{1-x}Zn_xS$ with g-C_3N_4 to achieve high photocatalytic activity and stability for hydrogen production.

To further enhance the photocatalytic activity of heterostructured photocatalysts, loading suitable cocatalysts to capture photo-induced charges and provide delicately designated sites for surface redox reaction is a useful approach [31–33]. However, most of the reported cocatalysts were noble metals (*e.g.* Pt and Au), and the main drawbacks of these cocatalysts are the scarcity and high cost, which will hamper the large-scale applications. Therefore, the development of efficient noble-metal-free photocatalysts that can be readily used for low-cost and pilot-system design have attracted much attention [33]. Thanks to the efforts of many groups, some efficient and non-precious cocatalysts have been developed [34,35]. Among them, Ni_2P has been reported as an efficient and earth-abundant cocatalyst to dramatically enhance photocatalytic activity [36,37]. Our recent work revealed that Ni_2P cocatalyst could boost hydrogen production over TiO_2, CdS, and C_3N_4 host photocatalysts, demonstrating its good catalytic property and general applicability [38].

Motivated by the above research, herein we prepare one-dimensional Ni_2P-$Cd_{0.9}Zn_{0.1}S$/g-C_3N_4 heterostructured photocatalysts for hydrogen production under visible-light irradiation. Detailed characterization on the morphology, structure, chemical state, and optical property of the composite photocatalysts was carried out. It is believed that the efficient spatial charge separation in the one-dimensional Ni_2P-$Cd_{0.9}Zn_{0.1}S$/g-C_3N_4 heterostructure could significantly improve the photocatalytic activity. The apparent quantum yield for hydrogen production can reach as high as 73.2% at 420 nm. Meanwhile, the g-C_3N_4 protective layer could effectively alleviate the photocorrosion of $Cd_{0.9}Zn_{0.1}S$, giving rise to good stability.

2. Experimental section

2.1. Synthesis procedure

All chemicals in the present study are of analytical grade and used as received without further purification. Fig. 1 shows the schematic illustration for the fabrication of one-dimensional Ni_2P-$Cd_{0.9}Zn_{0.1}S$/g-C_3N_4 heterostructure. The first step was to prepare $Cd_{0.9}Zn_{0.1}S$ nanorods *via* a facile hydrothermal method [39]. Typically, 18 mmol of $Cd(OAc)_2 \cdot 2H_2O$ and 2 mmol of $Zn(OAc)_2 \cdot 2H_2O$ were added into a 100 mL Teflon-lined autoclave, followed by addition of 30 mL of deionized water and 30 mL of ethylenediamine. The solution was stirred uniformly, and 25 mmol of thioacetamide was then added. The autoclave was sealed and heated at 220 °C for 24 h. The products were collected and washed three times each with deionized water and ethanol. Then the precipitates were dried in a vacuum oven at 80 °C for 5 h.

Ni_2P-$Cd_{0.9}Zn_{0.1}S$ composites were prepared through a two-step hydrothermal method. 0.4 g of as-prepared $Cd_{0.9}Zn_{0.1}S$ was first dispersed in 60 mL of ethylenediamine under stirring, and then a calculated amount of $Ni(NO_3)_2 \cdot 6H_2O$ and red phosphorus (the

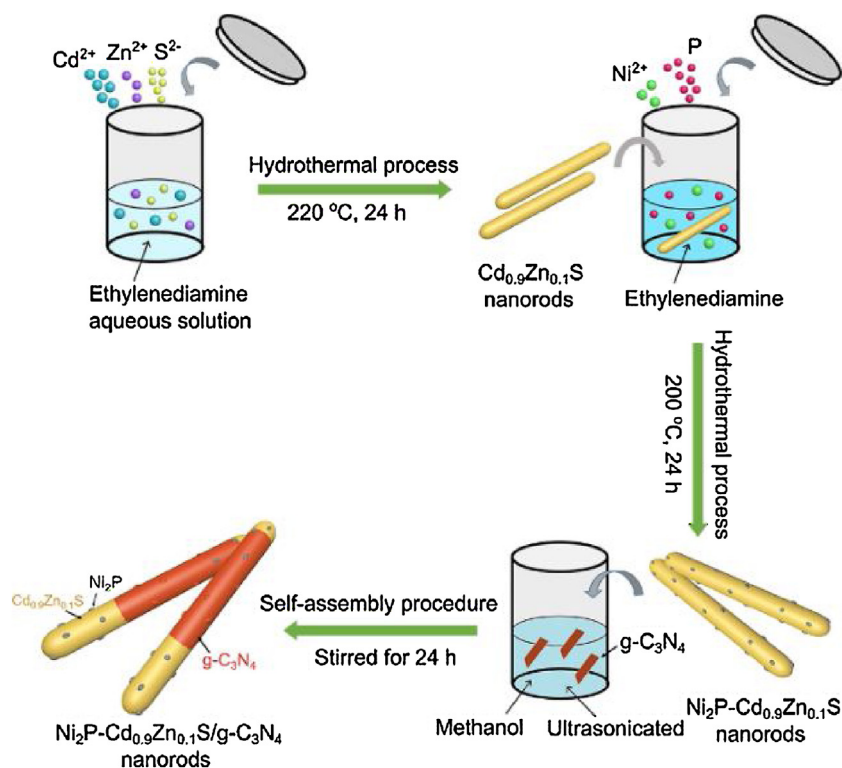**Fig. 1.** Schematic illustration for the fabrication of one-dimensional Ni_2P-$Cd_{0.9}Zn_{0.1}S$/g-C_3N_4 photocatalyst.

molar ratio of Ni to P is 1:5) were added. After stirring continuously for 30 min, the mixed solution was transferred into 100 mL Teflon-lined autoclave and maintained for 24 h at 200 °C. The products were collected and washed three times each with deionized water and ethanol. Then the precipitates were dried in a vacuum oven at 80 °C for 5 h.

The synthesis of g-C_3N_4 followed a reported annealing process [40]. 4.0 g of dicyandiamide and 0.2 g of barbituric acid were mixed in 20 mL of distilled water and heated at 90 °C with stirring until all water was evaporated. Then, the white product was calcined at 550 °C for 4 h in air, and ground into g-C_3N_4 powder.

Finally, ternary Ni_2P-$Cd_{0.9}Zn_{0.1}S$/g-C_3N_4 was prepared *via* a self-assembly procedure [41]. The as-prepared g-C_3N_4 was ground to fine power and then put into 20 mL of methanol. After being ultrasonically treated for 1 h to generate g-C_3N_4 nanosheets, Ni_2P-$Cd_{0.9}Zn_{0.1}S$ nanorods were added (the weight ratios of g-C_3N_4 to Ni_2P-$Cd_{0.9}Zn_{0.1}S$ were 0.5%, 2%, and 6%) and stirred for 24 h. After the residual methanol was evaporated by a rotary evaporator, the product was collected and dried in a vacuum oven at 40 °C for 5 h. The $Cd_{0.9}Zn_{0.1}S$/g-C_3N_4 sample was also prepared using a similar procedure for comparison.

2.2. Characterization

X-ray powder diffraction (XRD) patterns were measured by a PANalytical X'pert MPD Pro X-ray diffractometer. Scanning electron microscope (SEM) images were obtained by a JEOL JSM-7800F microscope. Transmission electron microscope (TEM) images were obtained using a FEI Tecnai G2 F30 S-Twin microscope attached with an OXFORD MAX-80 energy dispersive X-ray (EDX) system. X-ray photoelectron spectroscopy (XPS) measurements were carried out on a Kratos Axis-Ultra multifunctional X-ray spectrometer. All binding energies were referenced to the C 1 s peak at 284.8 eV. UV–visible (UV–vis) absorption spectra were acquired from a HITACHI U4100 spectrophotometer. The Fourier transform infrared spectrophotometer (FTIR) spectra were measured using a Bruker Vertex 70 FTIR spectrophotometer. The lock-in-based surface photovoltage (SPV) spectra were obtained using a surface photovoltage spectroscope. The measurement system consists of a source of monochromatic light (Omni-λ300), a lock-in amplifier (SR830) with a light chopper (SR540), and a sample chamber. Photoluminescence (PL) spectra for solid samples were measured using a PTI QM-4 fluorescence spectrophotometer with an excitation wavelength of 340 nm.

2.3. Photocatalytic measurement

Photocatalytic hydrogen production was performed in a side irradiation Pyrex cell with a magnetic stirring. Typically, 1.0 mg of as-prepared photocatalysts was added into 80 mL of aqueous solution containing Na_2S and Na_2SO_3 as sacrificial reagents. Before irradiation, nitrogen was purged through the reaction cell for 30 min to remove air in the dark. The reaction temperature was kept at 35 °C. A 300 W Xe-lamp equipped with a 420 nm cutoff filter was employed to provide the visible-light irradiation. The amount of generated hydrogen was measured by gas chromatography using a thermal conductivity detector (TCD). The average hydrogen production rates were calculated based on hydrogen generation amount in the first 5 h reaction. The apparent quantum efficiency (AQE) could be calculated according to Eq. (1). The turnover number (TON) and turnover frequency (TOF) were calculated by using Eqs. (2) and (3), respectively.

$$AQE\,(\%) = \frac{\text{The number of evolved hydrogen molecules} \times 2}{\text{The number of incident photons}} \times 100\% \tag{1}$$
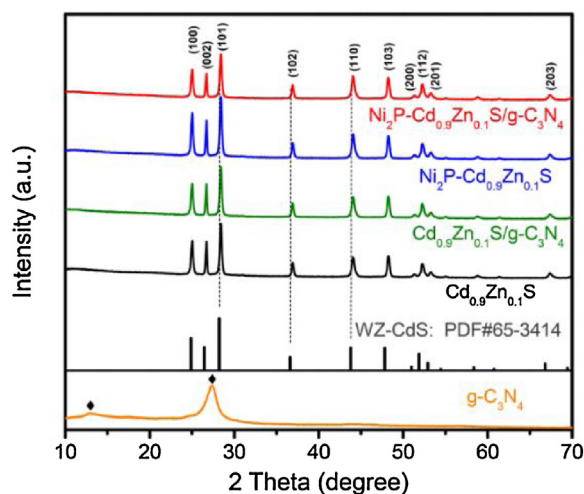

Fig. 2. XRD patterns of g-C_3N_4, $Cd_{0.9}Zn_{0.1}S$, $Cd_{0.9}Zn_{0.1}S$/g-C_3N_4, Ni_2P-$Cd_{0.9}Zn_{0.1}S$, and Ni_2P-$Cd_{0.9}Zn_{0.1}S$/g-C_3N_4.

$$TON = \frac{\text{Moles of evolved hydrogen}}{\text{Moles of } Ni_2P \text{ on photocatalyst}} \tag{2}$$

$$TOF = \frac{TON}{\text{Reaction time (h)}} \tag{3}$$

3. Results and discussion

3.1. Physicochemical properties of Ni_2P-$Cd_{0.9}Zn_{0.1}S$/g-C_3N_4 heterostructure

The crystal structures of as-prepared samples were determined by the XRD analysis. As shown in Fig. 2, two distinct diffraction peaks of pure g-C_3N_4 could be attributed to the graphitic phase with tri-s-triazine unit in its structure. The main diffraction peaks of $Cd_{0.9}Zn_{0.1}S$ were similar to those of wurtzite CdS (JCPDS no. 65-3414). Compared to CdS, the smaller radius of Zn^{2+} ions in $Cd_{0.9}Zn_{0.1}S$ resulted in the decreased interplanar spacing, which gave rise to the slight XRD peak shift toward higher degrees [42–44]. When coupling g-C_3N_4 and/or Ni_2P with $Cd_{0.9}Zn_{0.1}S$, no characteristic diffraction peaks for g-C_3N_4 or Ni_2P could be observed for the composite samples, probably due to their low amount and high dispersion. These results indicated that the modification of $Cd_{0.9}Zn_{0.1}S$ by g-C_3N_4 and Ni_2P did not alter the lattice structure of $Cd_{0.9}Zn_{0.1}S$.

To gain insight into the microstructures of Ni_2P-$Cd_{0.9}Zn_{0.1}S$/g-C_3N_4, the morphologies of as-prepared samples were characterized by SEM and TEM. As shown in Fig. 3a and b, Ni_2P-$Cd_{0.9}Zn_{0.1}S$/g-C_3N_4 exhibited one-dimensional nanorod morphology with an average diameter of ∼80 nm and a length of 0.5–1 µm. SEM and TEM images of single $Cd_{0.9}Zn_{0.1}S$ indicated that the one-dimensional morphology came from $Cd_{0.9}Zn_{0.1}S$ (Fig. S1). The detailed examination of TEM images of Ni_2P-$Cd_{0.9}Zn_{0.1}S$/g-C_3N_4 revealed that the ternary heterostructure displayed a core-shell structure consisting of a crystalline core of $Cd_{0.9}Zn_{0.1}S$ and a shell layer of g-C_3N_4 (Fig. 3b and c). The thickness of g-C_3N_4 layer was 5–10 nm. It was noted that Ni_2P nanoparticle with the size of around 10 nm was tightly deposited on the surface of nanorods. The HRTEM image revealed a lattice distance of 0.22 nm, which represents the (111) plane of hexagonal Ni_2P (Fig. 3d). However, more TEM images of Ni_2P-$Cd_{0.9}Zn_{0.1}S$/g-C_3N_4 uncovered that a part of one-dimensional nanorods were not completely covered by g-C_3N_4 layer (Fig. S2). In the present study, bulk g-C_3N_4 was first ultrasonically treated to generate g-C_3N_4 nanosheets, which were then coupled with $Cd_{0.9}Zn_{0.1}S$ nanorods by a self-assembly route. The
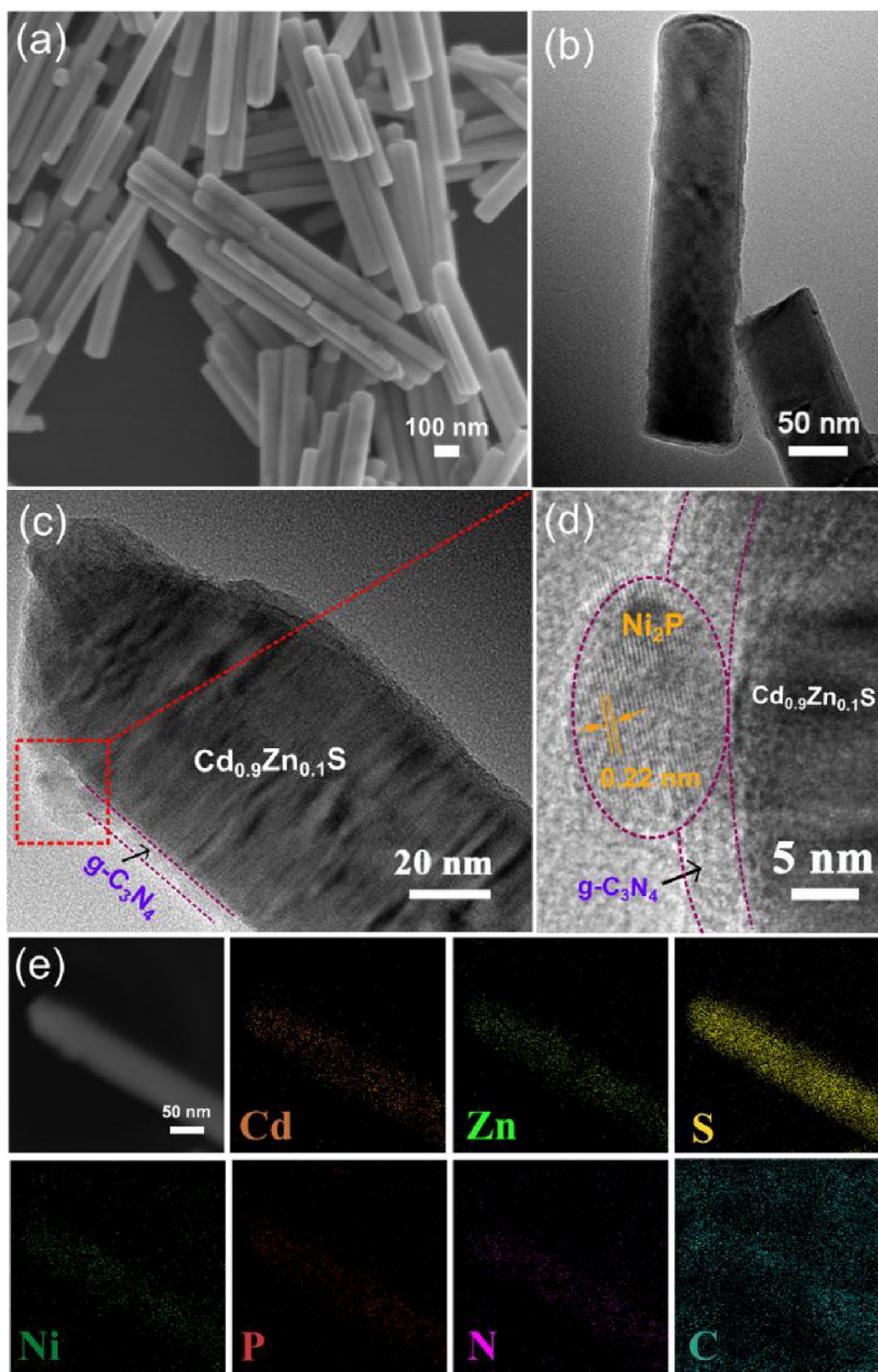
Fig. 3. (a) SEM image of $Ni_2P-Cd_{0.9}Zn_{0.1}S$. (b) TEM image of $Ni_2P-Cd_{0.9}Zn_{0.1}S$. (c and d) HRTEM images of $Ni_2P-Cd_{0.9}Zn_{0.1}S/g-C_3N_4$. (e) STEM image of $Ni_2P-Cd_{0.9}Zn_{0.1}S/g-C_3N_4$ and elemental mapping of Cd, Zn, S, Ni, P, N, and C species in $Ni_2P-Cd_{0.9}Zn_{0.1}S/g-C_3N_4$ (Excess C signals came from the carbon film on copper grids).

sizes of $Cd_{0.9}Zn_{0.1}S$ nanorods and $g-C_3N_4$ nanosheets might not have a good match, which should lead to the partly covered morphology. In addition, the low amount of $g-C_3N_4$ (the weight ratio of $g-C_3N_4$ to $Ni_2P-Cd_{0.9}Zn_{0.1}S$ was 2%) could be another reason. The TEM images of $Ni_2P-Cd_{0.9}Zn_{0.1}S/g-C_3N_4$ samples with different amount of $g-C_3N_4$ were thus measured. As shown in Fig. S3, when the weight ratio of $g-C_3N_4$ to $Ni_2P-Cd_{0.9}Zn_{0.1}S$ was 0.5%, $Ni_2P-Cd_{0.9}Zn_{0.1}S$ nanorods were almost uncovered by $g-C_3N_4$ layer.

When the weight ratio of $g-C_3N_4$ to $Ni_2P-Cd_{0.9}Zn_{0.1}S$ was increased to 6%, $Ni_2P-Cd_{0.9}Zn_{0.1}S$ nanorods were completely covered by $g-C_3N_4$ layer. To determine the composition and element distribution of $Ni_2P-Cd_{0.9}Zn_{0.1}S/g-C_3N_4$ nanorods, EDX element mapping was carried out. As shown in Fig. 3e, $Ni_2P-Cd_{0.9}Zn_{0.1}S/g-C_3N_4$ exhibited spatial distribution of Cd, Zn, S, Ni, P, C, and N species. It was found that Ni_2P nanoparticles and $g-C_3N_4$ layer were uniformly distributed on the surface of $Cd_{0.9}Zn_{0.1}S$ nanorods.
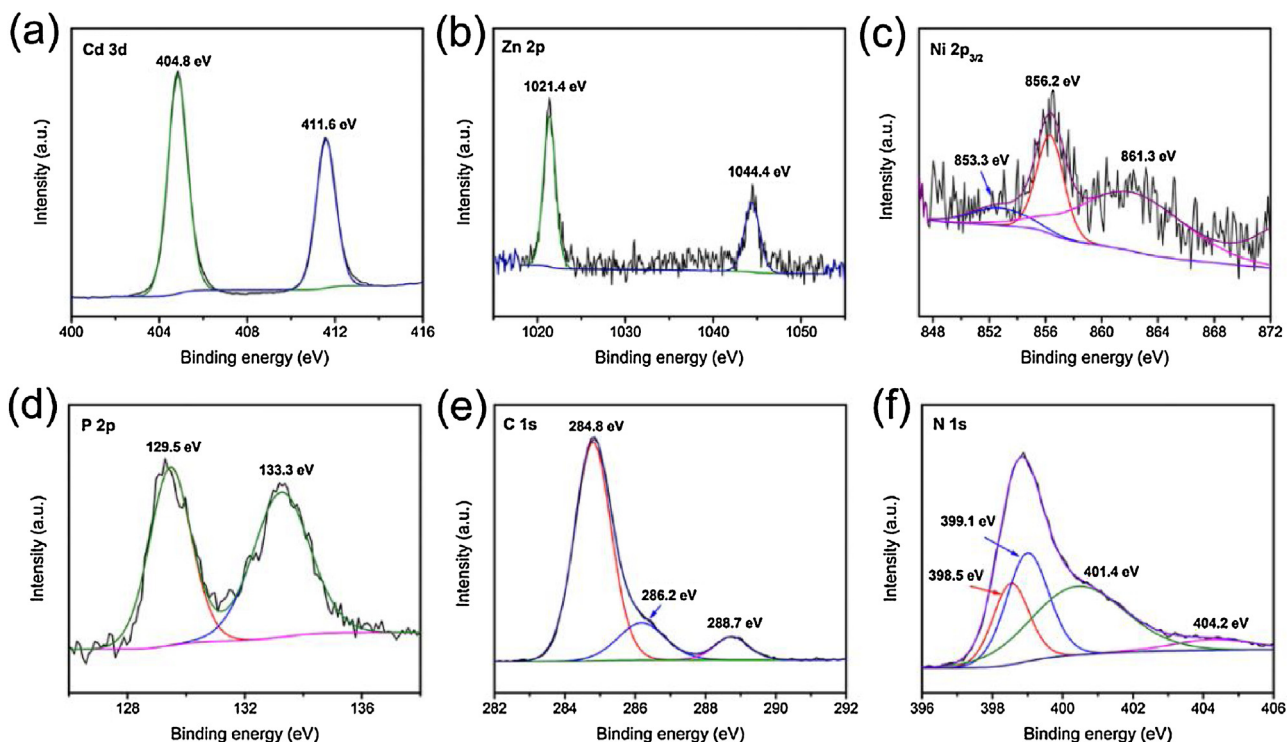
Fig. 4. XPS spectra of $Ni_2P-Cd_{0.9}Zn_{0.1}S/g-C_3N_4$. (a) Cd 3d; (b) Zn 2p; (c) Ni $2p_{3/2}$; (d) P 2p; (e) C 1s; (f) N 1s.

XPS measurements were performed to investigate the surface chemical states of $Ni_2P-Cd_{0.9}Zn_{0.1}S/g-C_3N_4$. As shown in the XPS spectrum of Cd 3d (Fig. 4a), two peaks at 404.8 and 411.6 eV were assigned to Cd $3d_{5/2}$ and Cd $3d_{3/2}$, respectively [45]. The binding energies for Zn $2p_{3/2}$ and Zn $2p_{1/2}$ were 1021.4 and 1044.4 eV (Fig. 4b), which confirmed the presence of Zn^{2+} ions [46]. Fig. 4c shows the XPS spectrum of Ni $2p_{3/2}$. The peak at 853.3 eV was assigned to $Ni^{\delta+}$ of Ni_2P, and the other peak at 856.2 eV corresponded to surface oxidation state [47]. In the P 2p spectrum (Fig. 4d), the peak at 129.5 eV was attributed to $P^{\delta-}$ of metal phosphides, while the peak at 133.3 eV arose from oxidized P species due to the air exposure [47]. As shown in Fig. 4e, the typical values for C—C, N—C≡N, and C—NH_2 of $g-C_3N_4$ were presented at binding energies of 284.8, 286.2, and 288.7 eV [48]. Meanwhile, the peaks at 398.5, 399.1, 401.4, and 404.2 eV of N 1 s spectrum (Fig. 4f) could be assigned to the binding energies of C—N≡C, N—$(C)_3$, C—N—H, and π excitations of $g-C_3N_4$ [49]. The XPS results further demonstrated the successful synthesis of $Cd_{0.9}Zn_{0.1}S$, Ni_2P, and $g-C_3N_4$ in the heterostructure. The element composition of $Cd_{0.9}Zn_{0.1}S$ in the heterogeneous system was also examined by XPS and EDX analysis. As shown in Table S1, the element composition of $Cd_{0.9}Zn_{0.1}S$ in $Ni_2P-Cd_{0.9}Zn_{0.1}S/g-C_3N_4$ was not changed compared to pure $Cd_{0.9}Zn_{0.1}S$.

Fig. 5 shows the FTIR spectra of the as-prepared samples. For $g-C_3N_4$ sample, the peak at $812\,cm^{-1}$ corresponded to aromatic C—N stretching. The prominent absorption bands at 1242, 1321, and $1411\,cm^{-1}$ could be assigned to the characteristic vibrations of C—NH—C units [30]. On the other hand, the peak of $Cd_{0.9}Zn_{0.1}S$ at $812\,cm^{-1}$ was assigned to the Cd-S stretching frequency and the band at $1090\,cm^{-1}$ corresponded to Zn-S vibration [50]. The absorption bands at 1242, 1321, and $1411\,cm^{-1}$ were distinctly observed in $Ni_2P-Cd_{0.9}Zn_{0.1}S/g-C_3N_4$, which indicated that $g-C_3N_4$ was successfully combined with $Ni_2P-Cd_{0.9}Zn_{0.1}S$.

UV-vis absorption spectra of as-prepared samples were presented in Fig. 6. The single $g-C_3N_4$ displayed a broad absorption feature from the ultraviolet to visible region compared with those in the literature [26]. Herein, $g-C_3N_4$ was synthesized by a reported copolymerization method [40]. During the copolymerization process, barbituric acid could introduce carbon atoms into the melon-based carbon nitride structures by replacing one of the ring nitrogen atoms, which changed the electronic structure of $g-C_3N_4$ and thus extended its optical absorption range. The composite samples showed almost the same absorption edges as that of pure $Cd_{0.9}Zn_{0.1}S$, implying that the elements of Ni_2P and $g-C_3N_4$ were not incorporated into the lattice of $Cd_{0.9}Zn_{0.1}S$. However, loading Ni_2P and $g-C_3N_4$ on the surface of $Cd_{0.9}Zn_{0.1}S$ led to increased absorption in the visible region. The band gaps of $Cd_{0.9}Zn_{0.1}S$ and $g-C_3N_4$ were respectively determined to be 2.49 and 2.57 eV from Tauc plots of $(\alpha h\nu)^n$ *vs.* photon energy $(h\nu)$ (Fig. S4), which were well consistent with the previous studies [39,40].
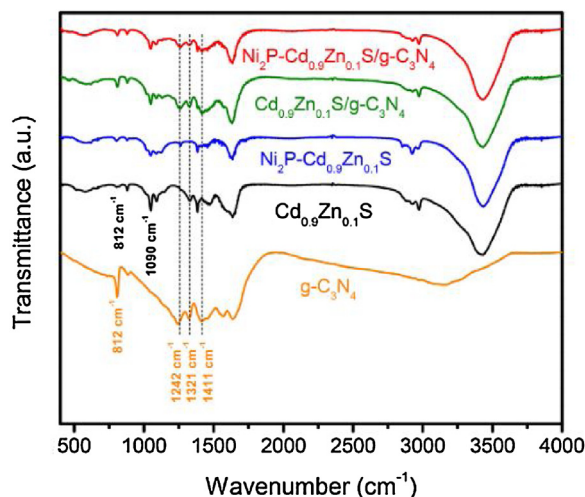

Fig. 5. FTIR spectra of $g-C_3N_4$, $Cd_{0.9}Zn_{0.1}S$, $Cd_{0.9}Zn_{0.1}S/g-C_3N_4$, $Ni_2P-Cd_{0.9}Zn_{0.1}S$, and $Ni_2P-Cd_{0.9}Zn_{0.1}S/g-C_3N_4$.
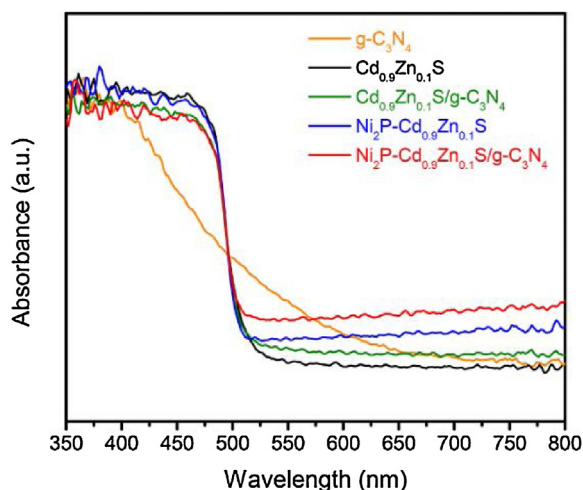
Fig. 6. UV–vis absorption spectra of g-C$_3$N$_4$, Cd$_{0.9}$Zn$_{0.1}$S, Cd$_{0.9}$Zn$_{0.1}$S/g-C$_3$N$_4$, Ni$_2$P-Cd$_{0.9}$Zn$_{0.1}$S, and Ni$_2$P-Cd$_{0.9}$Zn$_{0.1}$S/g-C$_3$N$_4$.
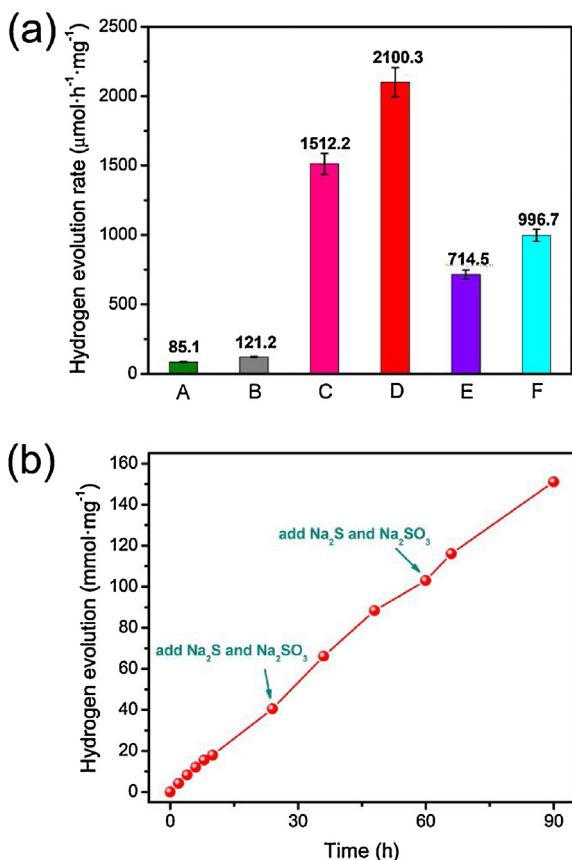
Fig. 7. (a) Comparison of photocatalytic hydrogen production over (A) Cd$_{0.9}$Zn$_{0.1}$S, (B) Cd$_{0.9}$Zn$_{0.1}$S/g-C$_3$N$_4$, (C) Ni$_2$P-Cd$_{0.9}$Zn$_{0.1}$S, (D) Ni$_2$P-Cd$_{0.9}$Zn$_{0.1}$S/g-C$_3$N$_4$, (E) physically mixed Ni$_2$P+Cd$_{0.9}$Zn$_{0.1}$S/g-C$_3$N$_4$, and (F) Pt-Cd$_{0.9}$Zn$_{0.1}$S/g-C$_3$N$_4$. (b) Long-term hydrogen production over Ni$_2$P-Cd$_{0.9}$Zn$_{0.1}$S/g-C$_3$N$_4$ for 90 h. Reaction condition: 1.0 mg photocatalyst, 0.75 M Na$_2$S and 1.05 M Na$_2$SO$_3$ in 80 mL of deionized water (180 mL for the stability test), 300 W Xe lamp equipped with a cutoff filter ($\lambda \geq 420$ nm).

3.2. Photocatalytic hydrogen production

The photocatalytic activities of as-prepared samples were investigated in Na$_2$S and Na$_2$SO$_3$ aqueous solution under visible-light irradiation. As shown in Fig. 7a, pure Cd$_{0.9}$Zn$_{0.1}$S showed rather low photocatalytic activity (85.1 μmol h^{-1} mg^{-1}),

and Cd$_{0.9}$Zn$_{0.1}$S/g-C$_3$N$_4$ showed higher photocatalytic activity (121.2 μmol h^{-1} mg^{-1}). Ni$_2$P cocatalysts could boost the photocatalytic hydrogen production over Cd$_{0.9}$Zn$_{0.1}$S and Cd$_{0.9}$Zn$_{0.1}$S/g-C$_3$N$_4$. With the optimal loading amount of Ni$_2$P (Fig. S5), Ni$_2$P-Cd$_{0.9}$Zn$_{0.1}$S/g-C$_3$N$_4$ showed the highest hydrogen production rate of 2100.3 μmol h^{-1} mg^{-1}, which was ~17 times higher than that of Cd$_{0.9}$Zn$_{0.1}$S/g-C$_3$N$_4$. Fig. S6 shows an action spectrum of Ni$_2$P-Cd$_{0.9}$Zn$_{0.1}$S/g-C$_3$N$_4$ for hydrogen production. The onset of the action spectrum agreed well with the absorption edge, which revealed that the visible-light-induced hydrogen production was due to the band-gap transition of Cd$_{0.9}$Zn$_{0.1}$S [51]. The apparent quantum yield for hydrogen production reaches as high as 73.2% using irradiation at 420 nm, which represents one of the highest values for noble-metal-free metal sulfide photocatalysts (Table S2).

For comparison, the activities of Pt-Cd$_{0.9}$Zn$_{0.1}$S/g-C$_3$N$_4$ and physically mixed Ni$_2$P+Cd$_{0.9}$Zn$_{0.1}$S/g-C$_3$N$_4$ were measured under the same condition (see Supporting Information). Although Pt cocatalysts enabled remarkable enhancement of photocatalytic activity, the hydrogen production rate of Pt-Cd$_{0.9}$Zn$_{0.1}$S/g-C$_3$N$_4$ was still much lower than that of Ni$_2$P-Cd$_{0.9}$Zn$_{0.1}$S/g-C$_3$N$_4$, indicating that Ni$_2$P was an excellent cocatalyst for promoting hydrogen production in the current system. The hydrogen production rate for physically mixed Ni$_2$P+Cd$_{0.9}$Zn$_{0.1}$S/g-C$_3$N$_4$ sample was much lower than that of Ni$_2$P-Cd$_{0.9}$Zn$_{0.1}$S/g-C$_3$N$_4$, revealing that the intimate contact between Ni$_2$P and Cd$_{0.9}$Zn$_{0.1}$S has a great effect on the performance. It was noted in Fig. S7 that the binding energies of Cd 3d, Zn 2p, and Ni 2p$_{3/2}$ for Ni$_2$P-Cd$_{0.9}$Zn$_{0.1}$S/g-C$_3$N$_4$ were the same as those for Cd$_{0.9}$Zn$_{0.1}$S and Ni$_2$P, indicating that the chemical bond was not formed between Ni$_2$P and Cd$_{0.9}$Zn$_{0.1}$S. Recent studies demonstrated that the intimate physical contact between Ni$_2$P and Cd$_{0.9}$Zn$_{0.1}$S should contribute to the enhanced photocatalytic performance [36]. Besides, the hydrogen production rates of Ni$_2$P-Cd$_{0.9}$Zn$_{0.1}$S/g-C$_3$N$_4$ with different amount of g-C$_3$N$_4$ were measured. As shown in Fig. S8, coating small amount of g-C$_3$N$_4$ substantially enhanced the hydrogen production activity. However, further increasing the content to 6% led to a reduction of the photocatalytic activity, probably due to the loss of active sites covered by g-C$_3$N$_4$ on the whole surface of Ni$_2$P-Cd$_{0.9}$Zn$_{0.1}$S. Meanwhile, with increased concentration of Na$_2$S and Na$_2$SO$_3$, the hydrogen production rate of Ni$_2$P-Cd$_{0.9}$Zn$_{0.1}$S/g-C$_3$N$_4$ initially increased and then underwent a decrease (Fig. S9). The hydrogen production reached a maximum in the presence of 0.75 M Na$_2$S and 1.05 M Na$_2$SO$_3$. When the concentration of the electron donors was further increased, the rate slightly decreased probably due to the loss of light blocked by the undissolved Na$_2$SO$_3$ particles [36].

To investigate the durability of Ni$_2$P-Cd$_{0.9}$Zn$_{0.1}$S/g-C$_3$N$_4$ photocatalyst, we carried out the photocatalytic experiment for 90 h (Fig. 7b). It is noticed that the hydrogen production rate had no significant decrease during the long-time test, indicating the good stability. XPS data of Ni 2p for Ni$_2$P-Cd$_{0.9}$Zn$_{0.1}$S/g-C$_3$N$_4$ samples before and after 90 h reactions were measured. As shown in Fig. S10, the valance state was not changed after the reaction, further demonstrating the stability of Ni$_2$P cocatalysts. Meanwhile, the morphology of Ni$_2$P-Cd$_{0.9}$Zn$_{0.1}$S/g-C$_3$N$_4$ photocatalysts after 90 h reaction was also not changed (Fig. S11). The turnover number (TON) of the photocatalytic system reached ~1,110,000 in 90 h with a turnover frequency (TOF) of 12,300 for Ni$_2$P.

3.3. Mechanism study

PL spectra of as-prepared samples were measured to explore light-induced charge transfer in the photocatalyst. As shown in Fig. 8a, pure g-C$_3$N$_4$ showed an extremely strong band edge emission at about 480 nm, corresponding to the band gap of g-C$_3$N$_4$. Single Cd$_{0.9}$Zn$_{0.1}$S showed a weak emission at about 500 nm and a broad emission at 420–440 nm. The emission at 500 nm should
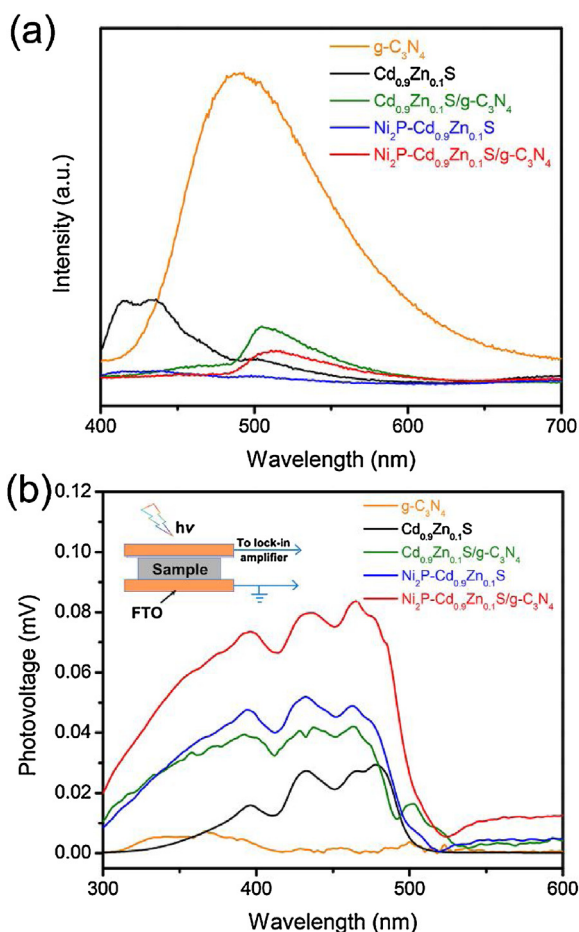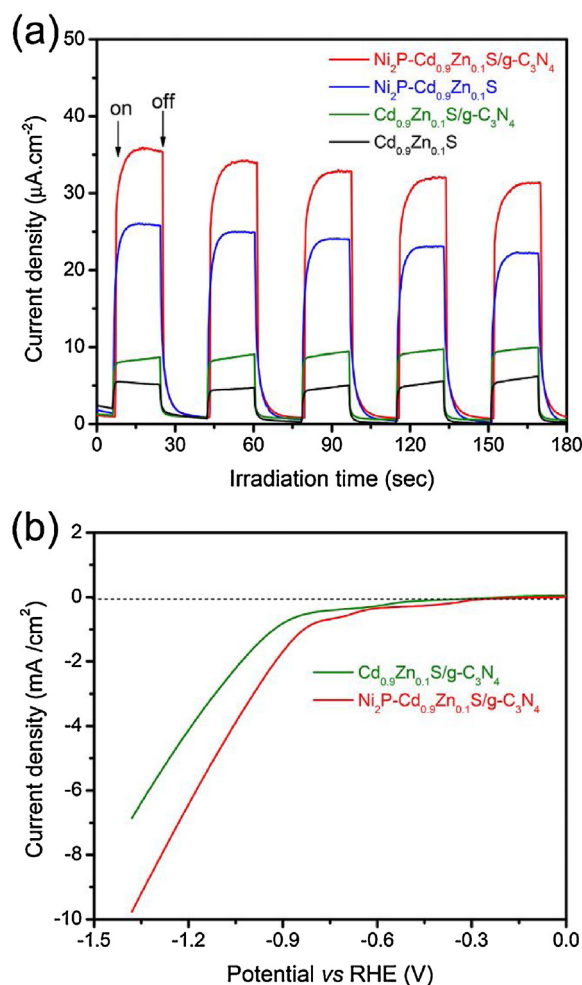
Fig. 8. (a) PL spectra and (b) SPV spectra (the inset shows the schematic setup for SPV measurement) of g-C_3N_4, $Cd_{0.9}Zn_{0.1}S$, $Cd_{0.9}Zn_{0.1}S/g$-C_3N_4, Ni_2P-$Cd_{0.9}Zn_{0.1}S$, and Ni_2P-$Cd_{0.9}Zn_{0.1}S/g$-C_3N_4.

Fig. 9. (a) Transient photocurrent responses of $Cd_{0.9}Zn_{0.1}S$, $Cd_{0.9}Zn_{0.1}S/g$-C_3N_4, Ni_2P-$Cd_{0.9}Zn_{0.1}S$, and Ni_2P-$Cd_{0.9}Zn_{0.1}S/g$-C_3N_4 measured at 1.1 V *vs.* RHE. (b) LSV curves for $Cd_{0.9}Zn_{0.1}S/g$-C_3N_4 and Ni_2P-$Cd_{0.9}Zn_{0.1}S/g$-C_3N_4. The electrochemical tests were carried out in N_2-saturated 0.5 M Na_2SO_4 solution. A 500 W xenon lamp coupled with an AM 1.5 filter was used as the light source.

be ascribed to the intrinsic band gap emission, and the broad emission could originate from ZnS defects [29]. The main peak of $Cd_{0.9}Zn_{0.1}S/g$-C_3N_4 composite shifted to about 520 nm, compared to bare $Cd_{0.9}Zn_{0.1}S$ and g-C_3N_4. The red-shift emission demonstrated an electronic interaction between two phases. It was also noted that the emission intensity of $Cd_{0.9}Zn_{0.1}S/g$-C_3N_4 was much lower than bare g-C_3N_4, indicating a better separation of photo-induced charges [52–54]. Compared to $Cd_{0.9}Zn_{0.1}S$ and $Cd_{0.9}Zn_{0.1}S/g$-C_3N_4, Ni_2P-$Cd_{0.9}Zn_{0.1}S$ and Ni_2P-$Cd_{0.9}Zn_{0.1}S/g$-C_3N_4 showed apparently decreased PL intensities, revealing that loading Ni_2P cocatalyst could facilitate the charge transfer so as to inhibit the charge recombination. From the PL analysis, it could be inferred that constructing the Ni_2P-$Cd_{0.9}Zn_{0.1}S/g$-C_3N_4 heterostructure is a useful route to promote charge separation.

The lock-in-based SPV spectra were also carried out to reveal the transfer properties of the photo-induced charge carriers. The signal of SPV can be attributed to the variation of surface potential barriers during the light irradiation, which can identify the light-responsive wavelength range and the separation efficiency of the electron-hole pairs in the photocatalysts [55]. As shown in Fig. 8b, positive photovoltage responses ranging from 300 to 500 nm were observed for g-C_3N_4 and $Cd_{0.9}Zn_{0.1}S$, indicating that both of them are n-type semiconductors [56]. The photovoltage of $Cd_{0.9}Zn_{0.1}S/g$-C_3N_4 obviously increased compared to pure g-C_3N_4 and $Cd_{0.9}Zn_{0.1}S$, indicating more efficient photo-induced charge separation in $Cd_{0.9}Zn_{0.1}S/g$-C_3N_4 composite [57]. After loading Ni_2P, the response signals of $Cd_{0.9}Zn_{0.1}S$ and $Cd_{0.9}Zn_{0.1}S/g$-C_3N_4

were obviously enhanced. In particular, the Ni_2P-$Cd_{0.9}Zn_{0.1}S/g$-C_3N_4 heterostructure showed the highest SPV signal, indicating the most efficient charge separation.

The charge separation behavior was further investigated through the transient photocurrent experiments (see Supporting Information). As shown in Fig. 9a, $Cd_{0.9}Zn_{0.1}S$ showed a very low photocurrent response, indicating the inefficient charge separation. Coupling g-C_3N_4 and/or Ni_2P was an effective route to improve photocurrent densities of $Cd_{0.9}Zn_{0.1}S$. It could be observed that the ternary Ni_2P-$Cd_{0.9}Zn_{0.1}S/g$-C_3N_4 exhibited the highest photocurrent density, suggesting a noticeable improvement in the suppression of charge recombination [58], which was in good agreement with the PL and SPV results. To achieve high activity, a photocatalytic system should also own rapid surface reaction. Linear sweep voltammetry (LSV) was measured to examine the catalytic abilities of $Cd_{0.9}Zn_{0.1}S/g$-C_3N_4 and Ni_2P-$Cd_{0.9}Zn_{0.1}S/g$-C_3N_4 for hydrogen production (see Supporting Information). As shown in Fig. 9b, $Cd_{0.9}Zn_{0.1}S/g$-C_3N_4 showed an onset potential of ca. −0.43 V *vs.* RHE for the reduction of protons, and Ni_2P-$Cd_{0.9}Zn_{0.1}S/g$-C_3N_4 exhibited a more positive onset potential at around −0.31 V *vs.* RHE. This positive shift indicated that the catalytic reductive ability of $Cd_{0.9}Zn_{0.1}S/g$-C_3N_4 was greatly enhanced by coupling Ni_2P [59]. Moreover, Ni_2P-$Cd_{0.9}Zn_{0.1}S/g$-C_3N_4 exhibited a significant improvement in current density beyond −0.8 V *vs.* RHE and a lower
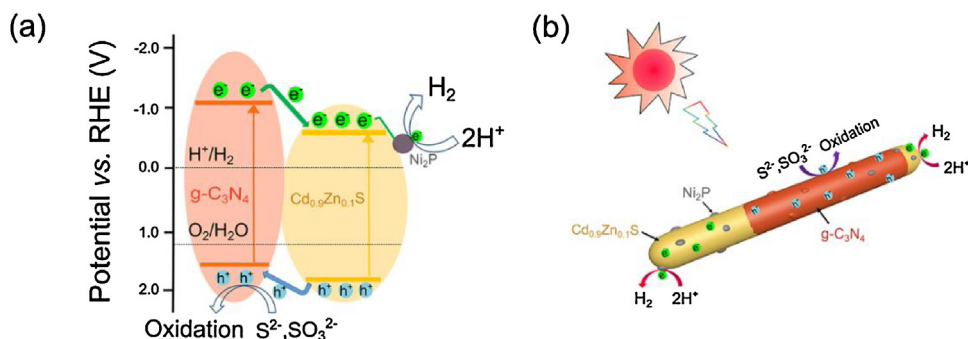
Fig. 10. Schematic illustration of (a) the band alignment and photo-induced charge transfer process in $Ni_2P-Cd_{0.9}Zn_{0.1}S/g-C_3N_4$, and (b) photocatalytic hydrogen production process over $Ni_2P-Cd_{0.9}Zn_{0.1}S/g-C_3N_4$.

overpotential to drive $6\,mA\,cm^{-2}$ than $Cd_{0.9}Zn_{0.1}S/g-C_3N_4$, further proving that Ni_2P could accelerate the surface reaction for proton reduction. On the basis of the above discussion, it can be summarized that the efficient separation of photo-induced charge carriers and improved surface reaction rate by Ni_2P cocatalyst cooperatively lead to a significantly improved photocatalytic activity for heterostructured $Ni_2P-Cd_{0.9}Zn_{0.1}S/g-C_3N_4$.

To better understand the improved charge separation efficiency of $Ni_2P-Cd_{0.9}Zn_{0.1}S/g-C_3N_4$, the band alignment of $Cd_{0.9}Zn_{0.1}S$ and $g-C_3N_4$ were investigated. Mott-Schottky plots were performed to investigate the electronic band structures of $Cd_{0.9}Zn_{0.1}S$ and $g-C_3N_4$. As shown in Fig. S12, the positive slopes of the Mott-schottky plots were observed, indicating the typical n-type characteristic of both $Cd_{0.9}Zn_{0.1}S$ and $g-C_3N_4$ [60]. The flat-band potentials of $Cd_{0.9}Zn_{0.1}S$ and $g-C_3N_4$ were estimated to be −0.45 and −0.81 V *vs.* RHE. In general, the conduction band potential (E_{CB}) for n-type semiconductor is about −0.2 V negative than its flat-band potential [61]. The E_{CB} values of $Cd_{0.9}Zn_{0.1}S$ and $g-C_3N_4$ were thus determined to be about −0.65 and −1.01 V *vs.* RHE. Since the band gaps (E_g) of $Cd_{0.9}Zn_{0.1}S$ and $g-C_3N_4$ were respectively 2.49 and 2.57 eV, the valence band potentials (E_{VB}) for $Cd_{0.9}Zn_{0.1}S$ and $g-C_3N_4$ were calculated to be 1.84 and 1.56 V *vs.* RHE [62]. Therefore, a type II band alignment was constructed for $Cd_{0.9}Zn_{0.1}S/g-C_3N_4$ heterostructure.

The schematic representation of the band alignment and photo-induced charge transfer process in $Ni_2P-Cd_{0.9}Zn_{0.1}S/g-C_3N_4$ is shown in Fig. 10a. Under visible-light illumination, photo-induced electrons in the conduction band (CB) of $g-C_3N_4$ can transfer to the CB of $Cd_{0.9}Zn_{0.1}S$, and the photo-induced holes in the valence band (VB) of $Cd_{0.9}Zn_{0.1}S$ can migrate to the VB of $g-C_3N_4$ due to the type II band alignment. Then the accumulated electrons in $Cd_{0.9}Zn_{0.1}S$ can be captured by Ni_2P cocatalysts, which behave as the active sites for proton reduction to generate hydrogen. Meanwhile, the accumulated holes in $g-C_3N_4$ layer can be effectively consumed by the sacrificial reagents (S^{2-}, SO_3^{2-}) (Fig. 10b). It is believed that the one-dimensional $Ni_2P-Cd_{0.9}Zn_{0.1}S/g-C_3N_4$ heterostructure has the following advantages to promote photocatalytic hydrogen production: i) introduction of both $g-C_3N_4$ and Ni_2P can lead to a spatial charge separation of photo-induced electrons and holes, thus greatly suppressing their recombination and increasing the lifetime; ii) Ni_2P nanoparticles can not only assemble the photo-induced electrons from $Cd_{0.9}Zn_{0.1}S$ but also act as reduction active sites to accelerate the reductive half-reaction; iii) one-dimensional nanostructure can facilitate charge transport and the large specific surface area can provide more reaction sites; iiii) the coated $g-C_3N_4$ layer can effectively collect the photo-induced holes from $Cd_{0.9}Zn_{0.1}S$, which substantially alleviates the photocorrosion of $Cd_{0.9}Zn_{0.1}S$ and enhances the stability for photocatalytic hydrogen production.

4. Conclusions

In summary, a novel one-dimensional $Ni_2P-Cd_{0.9}Zn_{0.1}S/g-C_3N_4$ heterostructured photocatalysts have been constructed, and their photocatalytic activity for hydrogen production has been examined under visible-light irradiation. The ternary $Ni_2P-Cd_{0.9}Zn_{0.1}S/g-C_3N_4$ photocatalysts achieved a dramatically enhanced activity, compared to single-component and binary-component photocatalysts. The apparent quantum yield reaches as high as 73.2% at 420 nm, which is one of the highest values for noble-metal-free metal sulfide photocatalysts. In addition to the advantages of one-dimensional morphology for photocatalytic reaction, it is believed that the efficient spatial separation of photo-induced charge carriers in $Ni_2P-Cd_{0.9}Zn_{0.1}S/g-C_3N_4$ heterostructure could significantly improve the photocatalytic activity. Meanwhile, the Ni_2P cocatalyst could promote the surface reaction and the $g-C_3N_4$ protective layer could effectively alleviate the photocorrosion of $Cd_{0.9}Zn_{0.1}S$, further enhancing the activity and stability of the photocatalysts. This work provides a new insight for the design and development of heterostructured photocatalysts with unique morphology and delicately controlled composition.

Appendix A. Supplementary data

Supplementary data associated with this article can be found, in the online version, at http://dx.doi.org/10.1016/j.apcatb.2017.06.018.

References

[1] A. Fujishima, K. Honda, Nature 238 (1972) 37–38.
[2] X. Chen, S. Shen, L. Guo, S.S. Mao, Chem. Rev. 110 (2010) 6503–6570.
[3] X. Chen, L. Liu, P.Y. Yu, S.S. Mao, Science 331 (2011) 746–750.
[4] G. Zhang, G. Liu, L. Wang, J.T.S. Irvine, Chem. Soc. Rev. 45 (2016) 5951–5984.
[5] H. Tong, S. Ouyang, Y. Bi, N. Umezawa, M. Oshikiri, J. Ye, Adv. Mater. 24 (2012) 229–251.
[6] K. Zhang, L. Guo, Catal. Sci. Technol. 3 (2013) 1672.
[7] A. Kudo, Y. Miseki, Chem. Soc. Rev. 38 (2009) 253–278.
[8] T. Hisatomi, J. Kubota, K. Domen, Chem. Soc. Rev. 43 (2014) 7520–7535.
[9] Y. Chen, Z. Qin, X. Wang, X. Guo, L. Guo, RSC Adv. 5 (2015) 18159–18166.
[10] D. Wang, Z. Zou, J. Ye, Chem. Mater. 17 (2005) 3255–3261.
[11] H. Wang, L. Zhang, Z. Chen, J. Hu, S. Li, Z. Wang, J. Liu, X. Wang, Chem. Soc. Rev. 43 (2014) 5234–5244.

[12] H. Li, Y. Zhou, W. Tu, J. Ye, Z. Zou, Adv. Funct. Mater. 25 (2015) 998–1013.
[13] Y. Wang, Q. Wang, X. Zhan, F. Wang, M. Safdar, J. He, Nanoscale 5 (2013) 8326–8339.
[14] S.J.A. Moniz, S.A. Shevlin, D.J. Martin, Z. Guo, J. Tang, Energy Environ. Sci. 8 (2015) 731–759.
[15] F.X. Xiao, J. Miao, H.B. Tao, S.F. Hung, H.Y. Wang, H.B. Yang, J. Chen, R. Chen, B. Liu, Small 11 (2015) 2115–2131.
[16] Y. Xia, P. Yang, Y. Sun, Y. Wu, B. Mayers, B. Gates, Y. Yin, F. Kim, H. Yan, Adv. Mater. 15 (2003) 353–389.
[17] B. Weng, S. Liu, Z.R. Tang, Y.J. Xu, RSC Adv. 4 (2014) 12685–12700.
[18] J. Tian, Z. Zhao, A. Kumar, R.I. Boughton, H. Liu, Chem. Soc. Rev. 43 (2014) 6920–6937.
[19] M. Liu, D. Jing, Z. Zhou, L. Guo, Nat. Commun. 4 (2013) 2278.
[20] S. Xie, X. Lu, T. Zhai, J. Gan, W. Li, M. Xu, M. Yu, Y.M. Zhang, Y. Tong, Langmuir 28 (2012) 10558–10564.
[21] D. Jing, L. Guo, J. Phys. Chem. B 110 (2006) 11139–11145.
[22] L. Wang, Z. Yao, F. Jia, B. Chen, Z. Jiang, Dalton Trans. 42 (2013) 9976–9981.
[23] J. Zhang, J. Yu, M. Jaroniec, J.R. Gong, Nano Lett. 12 (2012) 4584–4589.
[24] B.B. Kale, J.O. Baeg, S.K. Apte, R.S. Sonawane, S.D. Naik, K.R. Patil, J. Mater. Chem. 17 (2007) 4297–4303.
[25] J. Zhang, Y. Wang, J. Jin, J. Zhang, Z. Lin, F. Huang, J. Yu, ACS Appl. Mater. Interfaces 5 (2013) 10317–10324.
[26] X. Wang, S. Blechert, M. Antonietti, ACS Catal. 2 (2012) 1596–1606.
[27] Y. Kang, Y. Yang, L.C. Yin, X. Kang, L. Wang, G. Liu, H.M. Cheng, Adv. Mater. 28 (2016) 6471–6477.
[28] G. Liu, G. Zhao, W. Zhou, Y. Liu, H. Pang, H. Zhang, D. Hao, X. Meng, P. Li, T. Kako, J. Ye, Adv. Funct. Mater. 26 (2016) 6822–6829.
[29] X. Wang, J. Chen, X. Guan, L. Guo, Int. J. Hydrogen Energy 40 (2015) 7546–7552.
[30] L. Yao, D. Wei, Y. Ni, D. Yan, C. Hu, Nano Energy 26 (2016) 248–256.
[31] Z. Qin, Y. Chen, X. Wang, X. Guo, L. Guo, ACS Appl. Mater. Interfaces 8 (2016) 1264–1272.
[32] K. Chang, Z. Mei, T. Wang, Q. Kang, S. Ouyang, J. Ye, ACS Nano 8 (2014) 7078–7087.
[33] J. Ran, J. Zhang, J. Yu, M. Jaroniec, S.Z. Qiao, Chem. Soc. Rev. 43 (2014) 7787–7812.
[34] J. Yang, D. Wang, H. Han, C. Li, Acc. Chem. Res. 46 (2013) 1900–1909.
[35] P. Du, R. Eisenberg, Energy Environ. Sci. 5 (2012) 6012–6021.
[36] Z. Sun, H. Zheng, J. Li, P. Du, Energy Environ. Sci. 8 (2015) 2668–2676.
[37] W.Z. Gao, Y. Xu, Y. Chen, W.F. Fu, Chem. Commun. 51 (2015) 13217–13220.
[38] Y. Chen, Z. Qin, Catal. Sci. Technol. 6 (2016) 8212–8221.
[39] F. Xue, W. Fu, M. Liu, X. Wang, B. Wang, L. Guo, Int. J. Hydrogen Energy 41 (2016) 20455–20464.
[40] J. Zhang, X. Chen, K. Takanabe, K. Maeda, K. Domen, J.D. Epping, X. Fu, M. Antonietti, X. Wang, Angew. Chem. Int. Ed. 49 (2010) 441–444.
[41] C. Pan, J. Xu, Y. Wang, D. Li, Y. Zhu, Adv. Funct. Mater. 22 (2012) 1518–1524.
[42] C. Xing, Y. Zhang, W. Yan, L. Guo, Int. J. Hydrogen Energy 31 (2006) 2018–2024.
[43] Q. Li, H. Meng, P. Zhou, Y. Zheng, J. Wang, J. Yu, J. Gong, ACS Catal. 3 (2013) 882–889.
[44] X. Zhang, Z. Zhao, W. Zhang, G. Zhang, D. Qu, X. Miao, S. Sun, Z. Sun, Small 12 (2016) 793–801.
[45] Y. Chen, L. Guo, J. Mater. Chem. 22 (2012) 7507–7514.
[46] Y. Chen, Z. Qin, X. Guo, X. Wang, L. Guo, Int. J. Hydrogen Energy 41 (2016) 1524–1534.
[47] Y. Shi, Y. Xu, S. Zhuo, J. Zhang, B. Zhang, ACS Appl. Mater. Interfaces 7 (2015) 2376–2384.
[48] Q. Liang, Z. Li, X. Yu, Z.H. Huang, F. Kang, Q.H. Yang, Adv. Mater. 27 (2015) 4634–4639.
[49] S.S. Yi, J.M. Yan, B.R. Wulan, S.J. Li, K.H. Liu, Q. Jiang, Appl. Catal. B 200 (2017) 477–483.
[50] G. Yellaiah, K. Hadasa, M. Nagabhushanam, J. Alloys Compd. 581 (2013) 805–811.
[51] I. Tsuji, H. Kato, A. Kudo, Angew. Chem. 117 (2005) 3631–3634.
[52] Z. Chen, S. Berciaud, C. Nuckolls, T.F. Heinz, L.E. Brus, ACS Nano 4 (2010) 2964–2968.
[53] X. Bai, L. Wang, R. Zong, Y. Lv, Y. Sun, Y. Zhu, Langmuir 29 (2013) 3097–3105.
[54] X. Bai, L. Wang, Y. Zhu, ACS Catal. 2 (2012) 2769–2778.
[55] C. Han, L. Wu, L. Ge, Y. Li, Z. Zhao, Carbon 92 (2015) 31–40.
[56] L. Bi, D. Xu, L. Zhang, Y. Lin, D. Wang, T. Xie, Phys. Chem. Chem. Phys. 17 (2015) 29899–29905.
[57] S. Cao, J. Low, J. Yu, M. Jaroniec, Adv. Mater. 27 (2015) 2150–2176.
[58] Z. Qin, Y. Chen, Z. Huang, J. Su, Z. Diao, L. Guo, J. Phys. Chem. C 120 (2016) 14581–14589.
[59] T.P.A. Ruberu, Y. Dong, A. Das, R. Eisenberg, ACS Catal. 5 (2015) 2255–2259.
[60] A. Ishikawa, T. Takata, J.N. Kondo, M. Hara, H. Kobayashi, K. Domen, J. Am. Chem. Soc. 124 (2002) 13547–13553.
[61] X. Li, J. Yu, J. Low, Y. Fang, J. Xiao, X. Chen, J. Mater. Chem. A 3 (2015) 2485–2534.
[62] Y. Chen, Z. Qin, T. Chen, J. Su, X. Feng, M. Liu, RSC Adv. 6 (2016) 58409–58416.